Astronomy
&
Astrophysics

Self-consistent modeling of the outflow from the O-rich Mira IRC –20197

K. S. Jeong[1,2,3], J. M. Winters[4,1], T. Le Bertre[1], and E. Sedlmayr[2]

[1] LERMA, UMR 8112, Observatoire de Paris, 61 Av. de l'Observatoire, 75014 Paris, France
[2] Technische Universität Berlin, Zentrum für Astronomie und Astrophysik, Sekr. PN 8-1, Hardenbergstr. 36, 10623 Berlin, Germany
[3] Deutsches Zentrum für Luft– und Raumfahrt, Institute of Space Sensor Technology and Planetary Exploration, Rutherfordstr. 2, 12489 Berlin, Germany
[4] IRAM, 300 rue de la Piscine, 38406 St. Martin d'Hères, France

Abstract. We present a self–consistent time–dependent model for the oxygen–rich Mira variable IRC –20197. This model includes a consistent treatment of the interactions among hydrodynamics, thermodynamics, radiative transfer, equilibrium chemistry, and heterogeneous dust formation with TiO_2 nuclei. The model is determined by the stellar parameters, stellar mass $M_\star = 1.3 \, M_\odot$, stellar luminosity $L_\star = 1.4 \times 10^4 \, L_\odot$, stellar temperature $T_\star = 2400$ K, and solar abundances of the elements. The pulsation of the star is simulated by a piston at the inner boundary where the velocity varies sinusoidally with a period of $P = 636$ d and an amplitude of $\Delta v_p = 8 \, \text{km s}^{-1}$. Based on the atmospheric structure resulting from this hydrodynamic calculation at different phases, we have performed angle– and frequency–dependent continuum radiation transfer calculations, which result in the spectral energy distributions at different phases of the pulsation cycle and in synthetic light curves at different wavelengths. These are in good agreement with the infrared observations of IRC –20197. The model yields a time averaged outflow velocity of 11.9 km s^{-1} and an average mass loss rate of $7.3 \times 10^{-6} \, M_\odot$ yr^{-1} which are in good agreement with the values derived from radio observations. Furthermore, the chemical composition of the resulting grains is discussed.

Key words. hydrodynamics – radiative transfer – stars: winds, outflows – stars: circumstellar matter – stars: AGB and post-AGB – stars: individual: IRC –20197

1. Introduction

The mass loss from stars is fundamental for their evolution as individuals, as well as for the chemical evolution of stellar systems. For the objects which are on the Asymptotic Giant Branch (AGB), it plays a key rôle by dominating their subsequent evolution (Olofsson 1999). It is in this phase that low and intermediate mass stars ($1 \leq M \leq 6$–$8 \, M_\odot$) contribute the most to the replenishment of the interstellar medium (Sedlmayr 1994). Low mass stars ($M \leq 0.8 \, M_\odot$) evolve too slowly to contribute significantly to the recycling of matter, whereas high mass stars ($M \geq 8 \, M_\odot$) which end their lives as supernovae are rare and contribute mainly in the early phases of stellar systems. It is therefore essential to estimate quantitatively the mass loss phenomenon from AGB stars.

An understanding of the mechanisms which drive their outflows is crucial to obtain a correct description of this phenomenon (Sedlmayr & Winters 1997). Dust grains form in the outer layer of the stellar atmosphere which is extended by pulsations. These grains interact with the radiation field

and, due to radiation pressure, drive a massive wind. The outflows from carbon–rich AGB stars are now well described with self–consistent models (e.g. Fleischer et al. 1992, 1995; Höfner et al. 1995; Winters et al. 1997, 2000).

Outflows from oxygen–rich (O–rich) AGB stars have been more difficult to treat. Höfner et al. (1998) have presented O-rich wind models without dust, focusing on the effect of radiation pressure on molecules for driving the stellar wind. They stress the fact that the outflow driven by radiation pressure on molecules is a likely scenario for luminous cool stars and also that driving by molecules becomes effective only in the case of levitation of material through the pulsation induced shock waves. However, dust has been known to be present around these stars and the observations with ISO have allowed to identify spectral features produced by various kind of silicates (e.g. Waters et al. 1996; Posch et al. 1999; Fabian et al. 2001). Therefore, we set out to study the effect of dust formation on O–rich outflows in the frame work of a self–consistent model (Jeong et al. 1999; Jeong 2000).

Using a simple description for the stellar wind, Gail & Sedlmayr (1998, 1998b, 1999) investigated the dust formation process and the composition of the dust grains in O–rich

Send offprint requests to: K. S. Jeong,
e-mail: Kyung.Jeong@obspm.fr

Table 1. Adopted observational results for IRC −20197.

$M_\star$ [$M_\odot$]	$L_\star$ [$L_\odot$]	$T_\star$ [K]	P [days]	d [pc]	L_{max} ([$L_\odot$])	L_{min} ([$L_\odot$])	v_{exp} [km s^{-1}]	$\dot{M}$ [$M_\odot$ yr^{-1}]
1.0–2.0	14 200	≤ 2600	636	1200	23 200	13 900	14.0	$7.0-9.0 \times 10^{-6}$

circumstellar shells. They demonstrated that the direct nucleation of abundant gas phase species seems unlikey, since their nucleation occurs at significantly lower temperatures than those derived from the observations. Therefore, they have considered Ti_xO_y and Al_xO_y as the most likely nuclei in M stars.

Our objective is to obtain a description for dust–forming O-rich AGB stars undergoing mass loss at a large rate ($\geq 10^{-6}\ M_\odot$ yr^{-1}). In this paper, we describe a consistent time dependent model which can explain the generation of a wind from such a star. We probe this model by doing a detailed comparison with a well observed O–rich AGB source, IRC −20197. Our approach is similar to the one of Winters et al. (1997) who probed their C–rich modeling on a prototypical source, AFGL 3068.

This paper is organized as follows. An overview of the observational data on IRC −20197 is given in Sect. 2 and a description of the modeling method in Sect. 3. We present and discuss the results of our modeling on IRC −20197, the radial structure of the circumstellar dust shell (CDS), chemical composition of the dust grains, light curves at different wavelengths, spectral energy distributions (SEDs), and spatial spectra in Sect. 4. Our conclusions are presented in Sect. 5.

2. The observational data

The trend relating infrared (IR) excess to pulsation period (De Gioia-Eastwood et al. 1981) indicates that the stellar pulsation is a factor that should be considered in the discussion of circumstellar shells around red giants. As a test source, we have selected a well observed long period variable which shows evidence of a substantial mass loss, IRC −20197 (≡ IW Hya ≡ IRAS 09429−2148 ≡ RAFGL 5259).

It was found originally as an IR source in the Two Micron Sky Survey and later identified as a late M type star showing TiO and VO molecular bands. Its optical counterpart is elongated indicating the presence of a companion, probably a main–sequence A or F star. Observations in the IR range showed the source to be variable with a period of ∼636 days (Le Bertre 1993). Its bolometric lightcurve has an amplitude of at least 1 mag, with a possible trend on a longer timescale (see Fig. 2 in Le Sidaner & Le Bertre 1993: hereafter Paper I). These properties and its galactic latitude (23°) clearly characterize it as an AGB star undergoing Mira-type variations. Using the Period-Luminosity relation for O-rich Miras (Feast 1996), Le Bertre & Winters (1998) evaluate its distance, d to 1200 pc ($L_\star \sim 14\,200\ L_\odot$). The observational data for IRC −20197 are given in Table 1.

In the IR range, its spectrum shows emission bands at 10 μm and 18 μm (e.g. IRAS 1986) which are usually ascribed to amorphous silicate grains. In the radio range the source has been detected in several SiO, CO, and OH lines. The CO lines

Table 2. Mass loss rates and distances from observations for IRC −20197. $\dot{M}$ ($d = 1200$ pc) is the scaled mass loss rate adopting a distance $d = 1200$ pc.

Ref.*	v_{exp} [km s^{-1}]	d [pc]	$\dot{M}$ [$M_\odot$ yr^{-1}]	$\dot{M}$ ($d = 1200$ pc) [$M_\odot$ yr^{-1}]
K90	14.0	840	3.7×10^{-6}	7.6×10^{-6}
LL93	14.0	1500	1.0×10^{-5}	7.2×10^{-6}
LFOP93	14.0	880	5.2×10^{-6}	9.7×10^{-6}
KYLJ98	13.6	900	4.2×10^{-6}	7.5×10^{-6}
LW98	14.0	1200	7.2×10^{-6}	7.2×10^{-6}

* K90 (Kastner 1990), LL93 (Le Sidaner & Le Bertre 1993), LFOP93 (Loup et al. 1993), KYLJ98 (Knapp et al. 1998), LW98 (Le Bertre & Winters 1998).

indicate molecular gas expanding at a velocity of ∼14 km s^{-1} (Zuckerman & Dyck 1986; Knapp et al. 1998).

The mass loss rate has been evaluated by several groups. From the modeling of the IR energy distribution done in Paper I, the mass loss rate was found as $1 \times 10^{-5}\ M_\odot$ yr^{-1} for a distance of 1500 pc assuming a gas-to-dust ratio of 100. Using the CO (2–1) line observations of Zuckerman & Dyck (1986), Loup et al. (1993) estimate $5.2 \times 10^{-6}\ M_\odot$ yr^{-1} for $d = 880$ pc, whereas the modeling of the same line by Kastner (1990) gives $3.7 \times 10^{-6}\ M_\odot$ yr^{-1} for $d = 840$ pc. From CO (3–2) line observations, Knapp et al. (1998) estimate $4.2 \times 10^{-6}\ M_\odot$ yr^{-1} with $d = 900$ pc. Adopting a distance of 1200 pc (Le Bertre & Winters 1998) from the Period-Luminosity relation for O-rich Miras, we rescaled those mass loss rates referred above (Table 2). These rescaled mass loss rates are in the range $7-9 \times 10^{-6}\ M_\odot$ yr^{-1}.

The present mass of the star is not known. However, the ZAMS mass should have been larger than the present mass of the companion ($1 < M/M_\odot \leq 2$). As IRC −20197 may have already lost ∼0.1 $M_\odot$ on the RGB and possibly more on the AGB, it is reasonable to assume a present mass in the range $1-2\ M_\odot$. With a spectral type M9, the stellar temperature should be lower than 2600 K (Perrin et al. 1998).

IRC −20197 is an evolved star of the disk population ($z = 470$ pc) with an initial mass larger than 1 $M_\odot$. We can therefore assume that it has abundances close to the solar ones and we will adopt C/O = 0.5. However, due to possible third dredge-up events, its atmosphere could be already enriched in carbon.

The energy distributions at two different phases (near maximum and minimum) from the observations obtained at 7 different epochs (Paper I) will be used also to constrain the modeling. They can be completed with the IRAS photometric data. The IRAS fluxes agree with the ground–based photometry acquired

close to maximum (see Fig. 8). As there are only 2 hours–confirmed sightings by IRAS, these fluxes and the LRS can be ascribed with confidence to the light maximum of the source. As in Paper I, the IRAS fluxes have been corrected assuming a color temperature of 1 000 K.

3. The modeling method

Describing the physical processes in a CDS requires a simultaneous solution of hydrodynamics, thermodynamics, chemistry, dust formation, and radiative transfer, due to their strong mutual coupling. Once solid particles are formed in the CDS, they influence the hydrodynamical, thermodynamical, and chemical structure of the dust forming atmosphere itself. Thus the existence of dust in the system leads to a strong, non–linear coupling among the different physical systems and consequently influences the local and global structure of the circumstellar shell.

The modeling method applied here to the CDS of IRC –20197 is, therefore, a consistent time dependent treatment of hydrodynamics, thermodynamics, equilibrium chemistry, dust formation including growth and evaporation, and radiative transfer.

3.1. Hydrodynamics

We consider a spherically symmetric atmosphere surrounding a pulsating red giant characterized by its mass $M_\star$, effective temperature $T_\star$, luminosity $L_\star$, and the photospheric element abundances ε_i. In order to simulate the interior pulsation of the star, we apply a sinusoidal variation of the velocity with amplitude Δv_p and period P at the inner boundary r_i of the model. The models are, therefore, defined by the prescription of the 4 fundamental stellar parameters $(M_\star, L_\star, T_\star, \varepsilon_i)$ and of the 2 pulsation parameters $(P, \Delta v_p)$. $L_\star$ and $T_\star$ vary in time during the calculation and therefore, we will refer to their values in the hydrostatic initial model as $L_0 = L_\star(t = 0)$ and $T_0 = T_\star(t = 0)$. The initial stellar radius $R_0 = R_\star(t = 0)$ then follows from the Stefan–Boltzmann law. We start the calculation with a hydrostatic initial model and the velocity amplitude of the piston is increased slowly until the maximum value Δv_p is reached. Due to the sinusoidal variation of the velocity at the inner boundary, the location of r_i itself varies sinusoidally around its rest position $r_0 = r_i(t = 0)$ with amplitude $\Delta r_i = \Delta v_p P/2\pi$. During the calculation, the stellar mass is taken to be constant, i.e. variations on the evolutionary time scale are excluded. The models presented here are typically calculated for $160\,P$ of which the first $120\,P$ are needed to obtain a relaxed shell structure which extends out to $40\,R_0$. We use 512 radial mesh points for the numerical grid and a typical time step is of the order of 10^3 s, resulting in 5.5×10^4 time steps per period $(P = 636$ d). On a Cray T94 vector machine, one model run over $160\,P$ takes about 50 hours of CPU time. This is about a factor 5 longer than for a comparable C-rich model, caused by the larger diversity of relevant gas phase molecules and dust growth species which have to be considered in the O–rich case. Details of the hydrodynamic modeling and the basic equations are given in Fleischer et al. (1992) and Winters et al. (1997, 2000).

3.2. Chemistry

To calculate the formation of dust, it is essential to know the chemical composition of the gas phase, i.e. the concentration of the relevant atoms and molecules. The general way of calculating the chemical composition of the gas is the solution of a system of rate equations for all chemically relevant species, atoms, molecules, ions, and electrons (Goeres et al. 1988; Beck et al. 1992). However, the solution of this non–linear stiff set of differential equations requires a considerable amount of computing effort. Furthermore, enormous problems are associated with the input data needed for the calculation of the reaction rates which are often uncertain, if at all available. Therefore, we have chosen to assume chemical equilibrium and the concentrations of the species in the gas are, therefore, only functions of temperature, density, and chemical abundances ε_i.

A simple equilibrium chemistry may be applied if the expected deviations from this equilibrium have no crucial consequences for the results. Large non-equilibrium effects in red giants have to be expected, if either a rapid expansion of the medium leads to a frozen chemistry or if UV radiation from the interstellar radiation field or from a chromosphere are present (Beck et al. 1992). It is well known that late type giants later than about M5 do not have active chromospheres. Therefore, the UV radiation is only the photospheric field in the inner region of the envelope. Since the stars considered in this work are characterized by effective dust formation, the interstellar UV radiation field will be effectively absorbed in the outer regions of the envelope and will not affect the inner regions, where dust formation takes place. In this inner region, also the velocity fields are small, while deviations from kinetic equilibrium have to be expected in the wind regime. Therefore, at least in the dust formation zone, the assumption of an equilibrium chemistry seems to be justified.

Due to the high dissociation energy of the CO molecule ($\sim$11.2 eV), it is the first molecule formed and it cannot be easily destroyed. Therefore, in the case of an O–rich composition of the gas almost all carbon is locked up in this chemically inert molecule. Since nitrogen is mostly bound in N_2, the remaining oxygen is by far the most abundant element after hydrogen. Therefore, the chemistry in O–rich stars is dominated by water vapour and oxides of less abundant elements like Mg, Si, Al, Fe, and Ti. Consequently, in O–rich environments dust grains can only be formed from molecules containing the remaining oxygen and those heavy elements, which are contained in reactive gas phase species. In this case a heterogeneous composition of the emerging dust component has to be expected (Dominik et al. 1993). The molecules considered in our gas phase chemistry are given in Table 3.

In the gas phase, oxygen is mostly atomic at temperatures higher than 1500 K, but is essentially present in H_2O at temperatures lower than that temperature. The O_2 molecule is two orders of magnitude less abundant than O and OH. Silicon is mostly present as SiO, but the SiS molecule becomes dominant with decreasing temperatures, around 500 K. Magnesium is present in atomic form almost in the complete temperature range, but at around 600 K, MgOH becomes abundant. Iron is also in atomic form in the inner shell region, but at temperatures

Table 3. Molecules considered in the chemical equilibrium calculation.

Element	Molecules
H	H, H_2
C	CO
N	N, N_2
O	O, O_2, OH, H_2O
Si	Si, SiH, SiO
S	S, HS, SO, SiS, MgS, FeS, H_2S
Al	Al, AlH, AlOH, AlO_2H, Al_2O, Al_2O_3
Mg	Mg, MgH, MgO, MgOH
Fe	Fe, $Fe(OH)_2$
Ti	Ti, TiO, TiO_2

lower than $\sim 600\,$K, most Fe is in $Fe(OH)_2$. TiO_2 forms just after TiO becomes stable and therefore, their concentrations in the gas phase are rather comparable, until TiO_2 becomes dominant in the gas phase at temperatures lower than $1200\,$K.

3.3. Dust nucleation

Basically, the formation of dust grains can be considered as a two step process, *formation of a critical cluster* which serves as a condensation seed and *growth* of these clusters to macroscopic dust grains by addition of suitable molecules (Gail & Sedlmayr 1986). The formation of the critical cluster requires high supersaturation ratios ($S \gg 1$), whereas the growth process, i.e. condensation of the growth molecules on preexisting nucleation seeds proceeds already if $S > 1$, assuming thermodynamic and chemical equilibrium for the respective growth species (see Patzer et al. 1998 and Woitke 1999 for non–equilibrium effects).

Considering the abundance of the molecular species and the temperature at which they can exist in a solid phase, possible nucleation seed candidates are SiO, SiO_2, MgO, Fe, Al_2O_3, TiO, and TiO_2 and they will be considered separately in the following subsections. The formation of small clusters is the first step of the condensation process from the vapor. For studies of cluster formation, informations about thermodynamic and energetic properties, e.g. the Gibbs free energy of formation $\Delta_f G^\circ(N)$ and the binding energies of the clusters in the gas phase are required. Often experimental data are not available for the relevant molecular species and in this case, theoretical computation is the only possibility to obtain those quantities. In several cases, there exist theoretical calculations on thermodynamic properties of those clusters which have been considered as primary condensation seeds (e.g. John & Sedlmayr 1997; Köhler et al. 1997; Chang et al. 1998, 2000; Patzer et al. 1999; Jeong et al. 2000).

In order to determine the most likely primary condensation seed, nucleation rates $J_*/n_{<H>}$, i.e. the number of seed particles formed per second and per total number of hydrogen, have been calculated for these high temperature condensates (SiO, SiO_2, Fe, Al_2O_3, TiO, and TiO_2), assuming chemical equilibrium in the gas phase. In Fig. 1, contour levels of nucleation rates are plotted in the p–T plane in the range of

$\log(J_*/n_{<H>}) = [-33, -5]$ in steps of $\Delta \log(J_*/n_{<H>}) = 4$ for $\log(p\,[\text{dyne cm}^{-2}]) = [-16, 8]$ and $T[\text{K}] = [400, 1800]$ relevant to the CDS. Considering that the dust shells contain $\sim 10^{-13}$ dust grains per total number of hydrogen, typical values of nucleation rates relevant for CDS around O–rich AGB stars are in the range of $\log(J_*/n_{<H>}) = [-22, -14]$. Observations, e.g. Danchi et al. (1994) reveal that dust already exists at temperatures above $1000\,$K which indicates that the nucleation, the first step of dust formation, must occur at temperatures higher than $1000\,$K. The pressure at the inner edge of the CDS is typically in the range between $1\,\text{dyne cm}^{-2}$ and $10^{-2}\,\text{dyne cm}^{-2}$. Therefore, dust formation windows which are relevant to the inner region of a dust forming circumstellar shell around O–rich AGB stars are depicted in Fig. 1 by boxes, $\log(p\,[\text{dyne cm}^{-2}]) = [-2, 0]$ and $T\,[\text{K}] = [1000, 1200]$. In the following we discuss the possible primary condensates, based on investigations on cluster formation and on the calculation of nucleation rates represented by Fig. 1.

3.3.1. SiO

Due to the high bond strength and its high abundance in the gas phase, SiO has been regarded as favorable primary condensate (Nuth & Donn 1982; Gail & Sedlmayr 1986; Dominik et al. 1993). Although the SiO molecule is the most abundant candidate for nucleation in O–rich circumstellar shells, its nucleation rate only peaks around $600\,$K, which is significantly lower than the typical temperatures at the inner edge of the dust shells as derived e.g. from IR interferometry (Danchi et al. 1994). Consequently, SiO is not regarded here as a seed nucleus in O–rich CDS around AGB stars.

3.3.2. SiO_2

Since SiO_2 is considered as a solid species contributing to various dust features in the IR range (e.g. Posch et al. 1999; Speck et al. 2000), we performed calculations of the nucleation rate for this molecule. The nucleation rate of SiO_2 is negligible, $\log(J_*/n_{<H>}) < -35$ in the dust formation window. This is mainly because the SiO_2 molecule becomes abundant only at temperatures significantly lower than $1000\,$K. Therefore, the homogeneous nucleation of SiO_2 is not likely in O–rich CDS and we consider SiO_2 only as *growth species*.

3.3.3. MgO

Based on a modification of the classical Rittner potential model for alkali halide clusters (Rittner 1951), Köhler et al. (1997) calculated the thermodynamic properties for $(MgO)_N$ clusters ($N = 1-16$), using a semi-empirical interaction potential. In their calculations, the magnesium oxide is assumed to be a pure ionic compound formed from Mg^{2+} cations and O^{2-} anions, respectively. Based on their results for the thermodynamic properties of $(MgO)_N$ clusters, Köhler et al. determined the critical clusters for MgO nucleation and the corresponding cluster densities for a typical hydrogen number density of $n_{H_2} = 10^{10}\,\text{cm}^{-3}$ in the temperature range between $500\,$K and
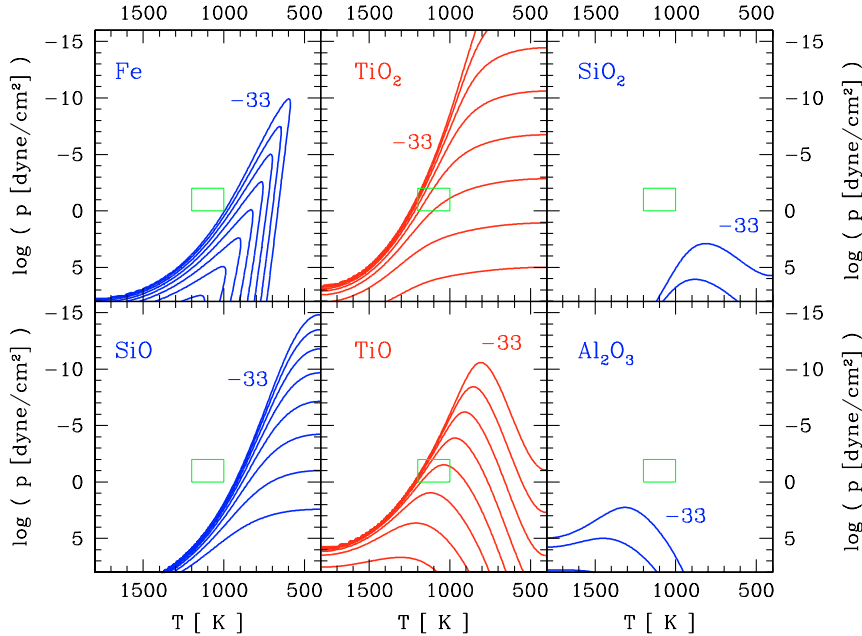
Fig. 1. Contour lines of the nucleation rates for different nucleating species in the $p-T$ plane. Contour levels are plotted in the range of $\log(J_*/n_{<H>}) = [-33, -5]$ in steps of $\Delta \log(J_*/n_{<H>}) = 4$. Dust formation windows are depicted by boxes which enclose densities and temperatures relevant to the inner region of dust shells around O-rich AGB stars.

1500 K where condensation is likely to occur. According to their results, the particle densities of the critical cluster are extremely low. Consequently, MgO nucleation is also completely negligible in CDS around O–rich AGB stars.

3.3.4. Fe

Iron is one of the most abundant elements having a stable condensate. From this abundance criterion, clustering of iron atoms has been considered to initiate the dust formation process (Gail & Sedlmayr 1986). Following the same method as for MgO clusters, John (1995) has calculated the formation rate for iron clusters up to $N = 19$. The binding energy for Fe_2 ($E_{bin} = 1.14$ eV) and Fe_3 ($E_{bin} = 2.96$ eV) is small and the equilibrium abundances of clusters with such a small dissociation energy are low at the relevant temperature (~1000 K) in the dust formation zone. Since the growth chain has to pass through the clusters Fe_2 and Fe_3 during the nucleation process, the nucleation of iron atoms can be relevant only well below 1000 K (John & Sedmayr 1997) and hence, Fe is not considered here as seed nucleus for dust grains in O–rich CDS.

3.3.5. Al₂O₃

Since Al_2O_3 is already stable at very high temperatures, it has been discussed as the first condensate in the cooling outflows of O–rich stars (Kozasa & Hasegawa 1987; Sedlmayr 1989; Onaka et al. 1989; Tielens 1990; Begemann et al. 1997; Nittler et al. 1997; Sogawa & Kozasa 1999).

Chang et al. (1998, 2000) have performed ab initio quantum mechanical calculations of Al_xO_y molecules which resulted in fully optimized molecular geometries, normal mode, and IR intensities at the Hartree–Fock and second order Møller–Plesset

frozen core level of approximation. Using the results of this investigation, Patzer et al. (1999) obtained the thermodynamic functions for the isomers of Al_2O_3 in the gas phase in the temperature range of 100 K–3000 K, which provide the quantities required for calculating the nucleation rates of Al_2O_3. Their chemical equilibrium calculations show that the concentration of the nominal molecule, Al_2O_3, is almost negligible in the relevant temperature range due to its low stability, although the supersaturation ratio of this molecule is high due to its small vapor pressure (Patzer et al. 1999). This investigation reveals that the most abundant aluminum compound in the gas phase is Al_2O_2 and that Al_2O_3 is virtually not present in the gas phase in the temperature range relevant for nucleation (Patzer 1998). Therefore, the *homogeneous* nucleation of molecular Al_2O_3 from the gas phase is unlikely in a circumstellar environment.

However, the analysis of meteorites reveals that corundum–bearing grains are in fact formed in the circumstellar shells of O–rich AGB stars (e.g. Zinner 1998). The formation of solid Al_2O_3 in principle might proceed via chemical reactions like $Al_2O + 2H_2O \rightarrow Al_2O_3 + 2H_2$ (e.g. Gail & Sedlmayr 1998) or $2Al + 3H_2O \rightarrow Al_2O_3 + 3H_2$ (Kozasa & Hasegawa 1987) which requires three body collisions and five body collisions, respectively. Such a scheme seems to be possible for the formation of corundum in a grain mantle, where the reaction partner can be adsorbed at the grain surface for a certain time. Therefore, in the following we consider Al_2O_3 only as a *growth species*.

3.3.6. TiO

The exclusion of possible abundant primary condensates (SiO, SiO_2, MgO, Fe, Al_2O_3) obliges us to search for other high temperature condensates, such as titanium oxides

(Gail & Sedlmayr 1999; Jeong et al. 1999), although the abundance of Ti is rather low. The TiO molecule forms already at high temperatures in the atmospheres of K and M stars due to its high bond energy of about 6.87 eV. In Fig. 1, only titanium oxides show nucleation rates corresponding to the dust formation window for O–rich AGB stars. However, in the dust formation window for O–rich CDS, the nucleation rate of TiO is typically in the range of $\log(J_*(TiO)/n_{<H>}) = [-15, -22]$, which is 4 orders of magnitude less than for TiO$_2$ ($\log(J_*(TiO_2)/n_{<H>}) = [-18, -12]$), because most Ti atoms are bound in the TiO$_2$ molecule in the gas phase (Gail & Sedlmayr 1999; Jeong et al. 1999; Jeong 2000). Furthermore, an investigation of the $(TiO)_N$ cluster properties (Jeong 2000; Jeong et al. 2000) shows that the equilibrium abundance of TiO clusters becomes negligibly small with decreasing temperature. Therefore, TiO is less favorable than TiO$_2$ as seed nucleus in O–rich CDS.

3.3.7. TiO$_2$

The lack of the thermodynamical properties required for calculating the nucleation rate of TiO$_2$ demands again a theoretical approach. Using density functional theory with a basis set of all–electron split valence, Jeong et al. (2000) have performed calculations which result in equilibrium geometries, binding energies, and the vibrational frequencies of Ti$_x$O$_y$ clusters ($x = 1$–6, $y = 1$–12). This study allows to obtain the thermodynamical properties of the $(TiO_2)_N$ clusters, e.g. $\Delta_f G°(N)$, required to calculate the nucleation rate (Jeong 2000). This investigation on the equilibrium abundance of the $(TiO_2)_N$ clusters shows that TiO$_2$ clusters are very stable even at high temperatures, >1000 K. Furthermore, as already discussed in Sect. 3.3.6 and shown in Fig. 1, the nucleation rates of TiO$_2$ are much higher, typically 4 orders of magnitude, than TiO in the dust formation window for O–rich CDS and this strongly indicates that TiO$_2$ can serve as primary condensate in O–rich CDS.

Summary It is clearly shown in Fig. 1 that only the titanium oxides show substantial nucleation rates in the relevant range of the p–T plane corresponding to the inner edge of CDS around O–rich AGB stars. Furthermore, TiO$_2$ nucleation is by far more efficient than TiO nucleation, due to the higher molecular concentration of TiO$_2$. Therefore, we consider TiO$_2$ as seed nuclei in our calculations for the outflows from O–rich AGB stars.

3.4. Heterogeneous growth

The TiO$_2$ seed nuclei grow by accretion of those molecular species which can form a stable condensate under the thermodynamic conditions prevailing in the circumstellar environment. The respective monomer of these condensates does not necessarily have to exist in the gas phase, but may be formed by chemical reactions on the grain surface from the atoms and molecules present in the gas phase. Actual formation of such a solid compound requires that all the generalized supersaturation ratios of the contributing atomic and molecular species are larger than unity (Dominik et al. 1993).

In the case of compounds with a definite stoichiometric composition, the equilibrium densities of the molecules in the gas phase can be calculated as follows. Consider a solid particle $E_{s_1}^1 E_{s_2}^2 \cdots E_{s_j}^j$ consisting of a number of j chemical elements denoted by E^j. The $s_j, j = 1, \cdots, J$ are the stoichiometric coefficients of the solid. From thermodynamics the equilibrium between atoms in the gas and the solid may be expressed by

$$\prod_{j=1}^{J} p_{E^j}^{s_j} = (p°)^{\Sigma_j s_j} \cdot \exp\left\{ \frac{\Delta G_s - \sum_{j=1}^{J} s_j \Delta G(E^j)}{kT} \right\} \quad (1)$$

where ΔG_s is the Gibbs energy of the solid state per monomer and $\Delta G(E^j)$ is the Gibbs energy for the atoms in the gas phase. Both Gibbs energies are taken relative to their reference states. $p_{E^j}, j = 1, \cdots, J$ are the partial pressures of the atoms in the gas phase and $p°$ is the reference pressure.

The growth velocity χ of the dust grains can be written as

$$\chi = \sum_{i=1}^{I} \chi_i = \xi_A^d \sum_{i=1}^{I} \overset{\circ}{\omega}_i V_i = \xi_A^d \sum_i \omega_i(1 - S_i^{-1})V_i \quad (2)$$

where $\xi_A^d = \sqrt[3]{36\pi}$ for a spherical grain and V_i is the monomer volume of the species i. The supersaturation ratio $S_i = p_i(1)/p_v$, where $p_i(1)$ is the partial pressure of the condensing species in the gas phase and p_v is the vapor saturation pressure with respect to the dust temperature. $\omega_i = n_i v_i \sigma_i$, where n_i is the number density of the species in the gas phase and v_i is the relative velocity between the grain and the growth species. For a spherical dust grain at rest in a gas with kinetic temperature T, $v_i^2 = kT/(2\pi m_i)$ with the Boltzmann constant k and the mass of the species m_i. σ_i, the reaction probability, is the number of reactions divided by the number of collisions and depends on the properties of the molecule and on the interaction energy of the collision as well as on the grain temperature and the chemical composition of the grain surface.

The supersaturation ratio S_i indicates the direction of the net effect. If $S_i > 1$, $\chi_i > 1$ and the reaction leads to grain growth. If $S_i < 1$, the dust particles are eroded by the evaporation of the respective species. The growth species and the contributing molecules are given in Table 4.

3.5. Radiative transfer

To determine the equilibrium temperature the radiative transfer problem is solved in grey approximation in the hydrodynamic calculation, which of course does not yield the SED, the light curves, nor the surface brightness profiles of the dust shell model. Hence in a second step, we solve the frequency-dependent stationary radiative transfer equation in spherical geometry for given radial structures of the dust shell model, i.e. at fixed instants of time. Details of the radiative transfer calculations are given in Winters et al. (1994). The transfer processes considered are grey absorption and thermal emission of the gas and frequency-dependent absorption and thermal emission of the dust grains assuming the small particle limit of Mie theory (Winters et al. 1997).

Table 4. Condensing species and the molecules contributing to their formation.

Condensing species	Contributing molecules
Fe	Fe
FeO	O, Fe, O_2, FeO
Fe_2O_3	O, Fe, O_2, FeO
Fe_3O_4	O, Fe, O_2, FeO
MgO	O, Mg, O_2, MgO
SiO	O, Si, SiO
SiO_2	O, Si, O_2, SiO
$MgSiO_3$	O, Si, Mg, O_2, SiO, MgO
$MgSiO_4$	O, Si, Mg, O_2, SiO, MgO
Al_2O_3	O, Al, O_2, Al_2O
Al_2SiO_5	O, Al, Si, O_2, SiO, Al_2O
$Al_6Si_2O_{13}$	O, Al, Si, O_2, SiO, Al_2O
$MgAl_2O_3$	O, Si, Mg, O_2, SiO, MgO
MgS	S, Mg, MgS
SiS	S, Si, SiS
Al_2S_3	Al, S
$MgSO_4$	O, Mg, S, O_2, MgO, MgS
TiO	O, Ti, TiO
TiO_2	O, Ti, TiO, TiO_2
Ti_2O_3	O, Ti, TiO, TiO_2
Ti_3O_4	O, Ti, TiO, TiO_2
$MgTiO_3$	O, Mg, Ti, MgO, TiO, TiO_2

In the small particle limit, the extinction coefficient of the dust component χ_ν^d is expressed by (Wickramasinghe 1972; Gail et al. 1984)

$$\chi_\nu^d = \frac{6\pi}{\lambda} \mathrm{Im}\left\{ \frac{m(\nu)^2 - 1}{m(\nu)^2 + 2} \right\} L_3(r). \tag{3}$$

$L_3(r)$ represents the mean volume of the dust grains. It is the third moment of the size distribution function $f(V, r)$ of the dust particles defined by

$$L_3(r) = \int_{V_l}^{\infty} V f(V, r) \, \mathrm{d}V \tag{4}$$

where V_l is a lower limit volume of the dust particles of $\sim 10^{-21}$ cm^3, which corresponds to a size where the particles already show macroscopic properties (Platt 1956).

In their frequency–dependent radiative transfer calculations using a sparse opacity sampling method, Höfner (1999) and Höfner et al. (2003) have performed a study on the molecular bands from the levitated regions of the stellar atmosphere and their temporal evolution. The richness of the molecular lines in the infrared spectral region can substantially lower the radiative equilibrium temperature of the gas compared to grey models. This probably allows the formation of dust to take place already much closer to the central star.

3.6. Dust opacity

The dynamical structure and therefore, the wind properties, of the models presented here are strongly influenced by radiation pressure on dust. Since the coupling between radiation field
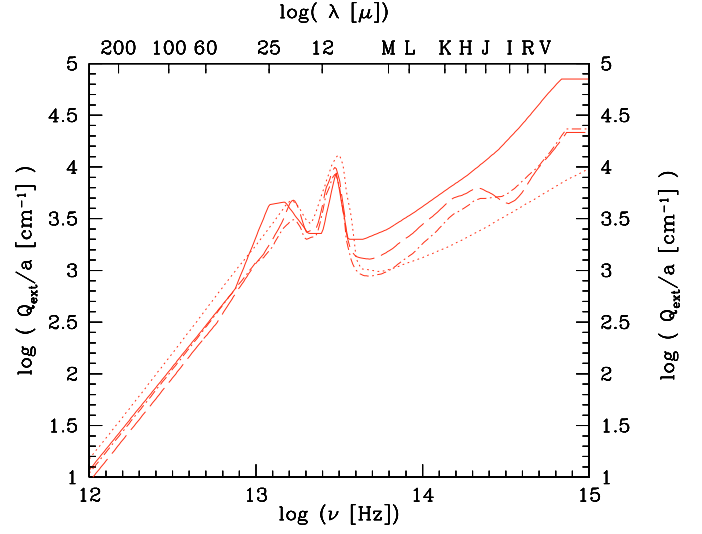

Fig. 2. Frequency-dependent extinction efficiencies for the Jones & Merrill (1976) data (solid line), for the Draine (1985) data (dotted line), for circumstellar silicates (dashed-dotted line) and for interstellar silicates (dashed line) from Ossenkopf et al. (1992).

and matter is provided by the local flux–mean extinction co-efficient $\chi_H(r)$, it has to be expected that the shell structure also depends on the optical properties of the grains. To describe the interaction between radiation and the grains resulting from our treatment of heterogeneous growth, we selected the optical properties for "astronomical silicate" calculated by Draine & Lee (1984) and tabulated in Draine (1985), the empirically determined efficiencies from Jones & Merrill (1976) in the revised version of Le Sidaner & Le Bertre (1996), and the optical constants for circumstellar and interstellar silicates calculated by Ossenkopf et al. (1992) using effective medium theory. The frequency-dependent extinction efficiencies resulting from these data sets are depicted in Fig. 2.

The most pronounced difference between the data sets of Jones & Merrill and of Draine & Lee occurs at wavelengths shortward to the 9.8 μm silicate feature. At these wavelengths, the Draine & Lee astronomical silicate is up to a factor of 10 more transparent than the Jones & Merrill silicate. Also, the ratio between the peak of the 9.8 μm feature and the neighbouring continuum towards shorter wavelengths is considerably smaller for the Jones & Merrill data set. The Ossenkopf et al. data sets show an intermediate behaviour for wavelengths shorter than 9.8 μm. At 9.8 μm and at wavelengths longer than 50 μm they resemble the values in the Jones & Merrill data set.

To calculate the hydrodynamic structure of the shell, the flux–mean extinction coefficient is replaced by its Planck–mean value. In Fig. 3 the corresponding Planck–mean extinction efficiencies are shown for the data sets.

The higher opacity at short wavelengths of the Jones & Merrill data transforms to considerably higher values of the respective Planck mean at high temperatures which even results in a different functional dependence on the temperature. Besides its obvious influence on the spectrum of the dust shell, the different optical properties therefore, might severely influence also the dynamical structure of the dust shell.
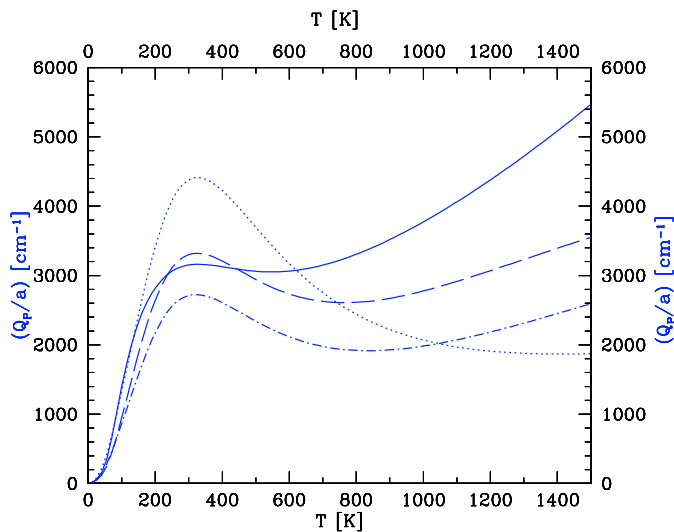
Fig. 3. Planck-mean extinction efficiencies for the Jones & Merrill (1976) data (solid line) and for the Draine (1985) data (dotted line), for circumstellar silicates (dashed-dotted line) and for interstellar silicates (dashed line) from Ossenkopf et al. (1992).

Due to the very different temperature dependence of the Planck–mean extinction efficiencies in particular in the inner region of the CDS where the dust forms and the wind is initiated, the resulting wind properties (mass loss rate, outflow velocity) of the corresponding models differ substantially (see models J42, J59, and J77 in Table 5). The outflow velocity as well as the mass loss rate are higher in the models calculated with the Jones & Merrill opacity than in the models with dust opacity of Draine & Lee and with dust opacity (circumstellar silicate) of Ossenkopf et al. The model with dust opacity of Ossenkopf et al. results in even smaller values of $\dot{M}$ and v_∞ than the model with Draine & Lee dust opacity. Interestingly, the dust-to-gas ratio remains virtually unaffected by the different optical constants. This is in contrast to the carbon-rich case, where mainly the dust-to-gas ratio and the velocity are affected by different opacities whereas the mass loss rate is rather insensitive to different optical constants (see Andersen et al. 1999; Fleischer et al. 1999; Winters et al. 2000).

Model calculations with Draine & Lee opacity and with dust opacity of Ossenkopf et al. do not provide results (outflow velocities, mass loss rates and simultaneously the SEDs and light curves) matching to those from the observations for IRC –20197. On the other hand, using the Jones & Merrill absorption efficiencies, we could get suitable models for IRC –20197. Therefore, in the following we will present models calculated with the Jones & Merrill opacity.

Circumstellar dust seems to undergo an alteration of chemical and structural nature after it is injected into the interstellar medium (ISM), which changes its optical properties (e.g. Woitke et al. 1993; Jones et al. 1996; Demyk et al. 2001). It is therefore not a surprise that the Draine & Lee grain model which has been constructed to fit the properties of the dust in the ISM does not provide proper results for describing the dust properties in the CDS of IRC –20197.

4. Results

In order to model IRC –20197, we performed 21 calculations with different parameter sets. For this object, stellar mass and effective temperature are not well constrained from the observations (see Table 1), whereas this is not the case for the other parameters. The parameters for the hydrostatic initial models and the resulting values from the 21 model calculations are given in Table 5.

The mean values of v_∞ and $\dot{M}$ in Table 5 have been calculated by averaging over a time interval of $\Delta t = 40P$ the radially averaged velocity and mass flux through all shells between $30R_0$ and $40R_0$. The mean value of the dust–to–gas mass ratio $< \rho^d/\rho^g >$ is obtained by averaging the ratio $\Sigma_i m_i n_i / 1.4 m_{<H>} n_{<H>}$ over the same Δt and the same shells, between $30R_0$ and $40R_0$. m_i is the mass of element i, n_i the number density of element i contained in dust grains, $n_{<H>}$ the total number density of hydrogen, and $m_{<H>}$ the mass of an hydrogen atom.

From the model results given in Table 5, it is clear that the mass loss rate depends sensitively on the stellar temperature and also on the stellar mass as in the C-rich case (Arndt et al. 1997; Winters et al. 2000; Wachter et al. 2002). Generally, mass loss rates and outflow velocities decrease with increasing stellar mass. However, for high stellar temperatures which are a critical criterion for the dust formation, their dependence on the stellar mass is strongly related to the combination with other parameters, such as the velocity amplitude Δv_p. Detailed investigations on the dependence of $\dot{M}$ and v_∞ on the fundamental parameters will be presented in a forthcoming paper (Jeong et al. 2003, in preparation).

The models with $T_0 \leq 2400$ K and $\Delta v_\infty = 8 \, \mathrm{km \, s^{-1}}$ provide values of mass loss rates and terminal velocities in the range observed for IRC –20197. However, the constraints of a model for IRC –20197 are not only the values given in Table 5, but also simultaneously, the observed SED and the observed lightcurves (Sect. 4.4). Considering all these constraints together, we have chosen model J42 as the best model for IRC –20197, since this model shows not only a good agreement of mass loss rate $\dot{M}$ and outflow velocity v_∞ with those derived from the observations, but also is in good agreement with the observed SEDs and light curves of IRC –20197.

4.1. Radial structure of the dust shell model

The radial structure of model J42 is shown in Fig. 4 at $t = 160.0P$ corresponding to an intermediate phase of the light curves. The radial structures of time–dependent O–rich models show characteristics similar to the C–rich case (see, e.g., Fleischer et al. 1992; Winters et al. 2000):

- The CDS exhibits a discrete layered structure. The dust is concentrated in discrete layers which can be seen for example in the degree of condensation of oxygen (dark solid line in the lower panel of Fig. 4).
- The dust layers are correlated with the hydrodynamic structure. This indicates that the strong shocks propagating through the shell are accelerated by radiation pressure on

Table 5. Parameters of the hydrostatic initial models and the resulting values of the time–dependent models; D (Draine 1985), JM (Jones & Merrill 1976), and OHM (Ossenkopf et al. 1992).

No.	dust opac.	$M_\star$ [$M_\odot$]	L_0 [$L_\odot$]	T_0 [K]	C/O	P [d]	Δv_p [km s^{-1}]	$\dot{M}$ [$M_\odot$ yr^{-1}]	v_∞ [km s^{-1}]	ρ^d/ρ^g [10^{-3}]	$K - L'$
J39	JM	1.2	14000	2300	0.50	636	8	7.6×10^{-5}	18.4	3.5	4.97
J40	JM	1.3	14000	2300	0.50	636	8	6.8×10^{-5}	15.9	3.5	3.76
J41	JM	1.4	14000	2300	0.50	636	8	4.7×10^{-5}	16.4	3.2	4.31
J47	JM	1.6	14000	2300	0.50	636	8	2.6×10^{-5}	17.6	3.3	3.32
J51	JM	1.2	14000	2350	0.50	636	8	6.2×10^{-5}	17.7	3.6	4.37
J38	JM	1.2	14000	2400	0.50	636	8	2.3×10^{-8}	1.9	3.7	1.20
J42	JM	1.3	14000	2400	0.50	636	8	7.3×10^{-6}	11.9	3.5	2.34
J45	JM	1.4	14000	2400	0.50	636	8	7.7×10^{-8}	4.9	1.5	1.27
J49	JM	1.5	14000	2400	0.50	636	8	4.4×10^{-5}	16.7	3.1	3.74
J48	JM	1.6	14000	2400	0.50	636	8	2.5×10^{-5}	17.5	3.1	3.32
J43	JM	1.3	14000	2500	0.50	636	8	5.0×10^{-8}	2.3	3.9	1.09
J50	JM	1.5	14000	2500	0.50	636	8	1.6×10^{-8}	1.6	2.1	1.11
J55	JM	1.2	14000	2400	0.50	636	9	5.5×10^{-5}	18.9	3.4	4.40
J57	JM	1.4	14000	2400	0.50	636	9	5.8×10^{-5}	19.2	3.7	4.67
J52	JM	1.2	14000	2400	0.50	636	10	9.1×10^{-5}	19.9	3.7	6.72
J44	JM	1.3	14000	2400	0.50	636	10	1.0×10^{-4}	16.4	3.9	7.04
J56	JM	1.3	14000	2450	0.50	636	10	1.1×10^{-4}	20.3	3.4	6.48
J54	JM	1.2	14000	2500	0.50	636	10	6.7×10^{-5}	20.8	3.3	4.90
J53	JM	1.3	14000	2500	0.50	636	10	3.5×10^{-7}	4.4	3.9	1.19
J59	D	1.3	14000	2400	0.50	636	8	1.4×10^{-7}	6.2	3.6	1.12
J77	OHM	1.3	14000	2400	0.50	636	8	1.2×10^{-8}	2.2	3.8	1.22

dust. These dust–induced shocks are discussed in detail in Fleischer et al. (1991, 1992). The shocks produce a distinct step–like density structure which in turn provides favorable conditions for dust growth.

- The temperature structure in the inner region is characterized by a *back–warming effect* by which the material below the dust layer is heated due to the thermal re–emission by the dust grains. This effect influences decisively the nucleation which strongly depends on temperature.

- The interaction between the dust opacity and the temperature structure leads to the so-called *exterior κ-mechanism* (Fleischer et al. 1995; Höfner et al. 1995) revealing an *eigenperiod* of the dust shell which is generally longer than the pulsation period of the star. In our pulsating models, this induces a multi-periodic behavior of the dust shell which is connected to a time scale of a few pulsation periods of the star.

The ratio α of radiative acceleration to the gravitational deceleration reaches high values and exceeds unity already close to the star (at $5 R_0$), which leads to a wind with $\dot{M} = 7.3 \times 10^{-6} M_\odot$ yr^{-1} and v_∞ = 11.9 km s^{-1}, in good agreement with the values derived from observations for IRC –20197. The final dust–to–gas ratio is $< \rho^d/\rho^g > = 3.5 \times 10^{-3}$. The inhomogeneous dust distribution in the CDS is also seen in the number of dust grains per total hydrogen density and in the mean grain radius. $n_d/n_{<H>}$ varies from 10^{-14} up to

10^{-11}, but has mostly a value of $\sim 10^{-13}$. The mean grain radius is $< r_d > = 0.05\,\mu$m, but the mean particle size can reach a value of $>0.3\,\mu$m in the inner shell region and of $0.2\,\mu$m locally in the outer shell region.

The radial structure of model J42 for IRC –20197 repeats its general characteristics after a time interval of ~ 5 P. This eigen–timescale can be seen in Figs. 9 and 11.

Concerning the influence of the dust opacity on the radial structures of the CDS, we compare the radial structure of model J42 to that of model J59 obtained with the same stellar parameters, but with Draine & Lee dust opacity (Fig. 5). Model J59 does not show a layered structure of the CDS, but a rather homogeneous dust distribution (see the course of α in the lower right panel of Fig. 5). Therefore, no radiation–driven shocks are induced and the velocity profile (outside of $5 R_0$) almost resembles that of a stationary wind. The velocity exceeds the escape velocity only at $23 R_0$ and drives a wind with low mass loss rate of $\dot{M} = 1.4 \times 10^{-7} M_\odot$ yr^{-1} and $v_\infty = 6.2$ km s^{-1}, much lower than the corresponding values derived from observations of IRC –20197. The average density of model J59 is one order of magnitude lower than that of model J42 and does not show discrete enhanced layers, which provides less favorable conditions for dust formation and growth. The average number of dust grains is only $n_d/n_{<H>} = 10^{-15}$, orders of magnitude lower than that of model J42. The mean radius of the dust particles is $0.025\,\mu$m, but reaches $0.6\,\mu$m in the inner shell region.
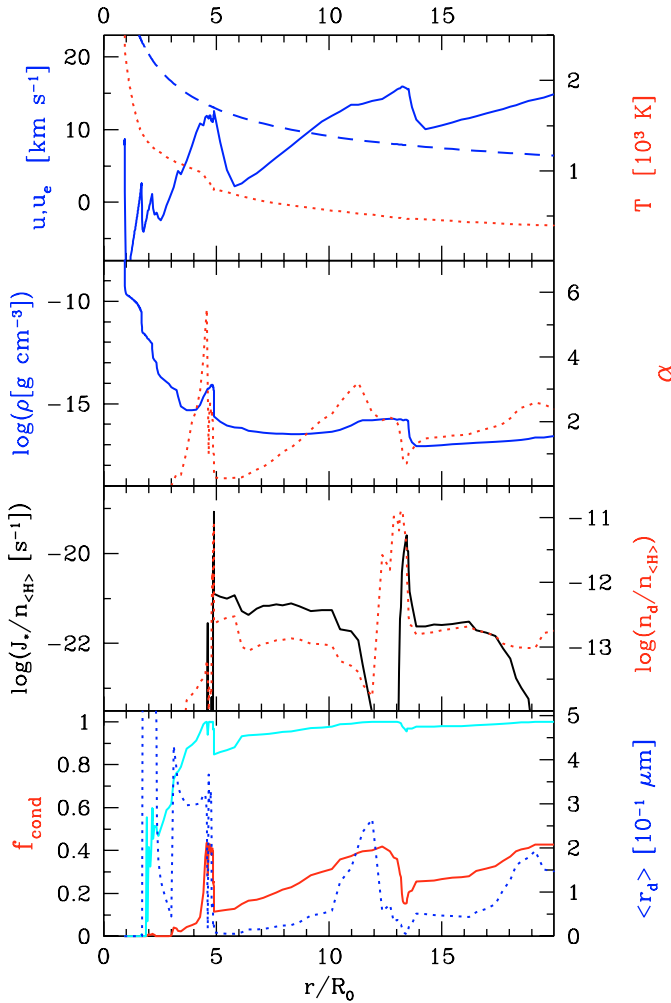
Fig. 4. Radial structure of the CDS model J42 at $t = 160.0$ P. Upper diagram: velocity (solid line), escape velocity (dashed line), and temperature structure (dotted line). **2nd** diagram: density ρ (solid) and radiative acceleration in units of the local gravitational deceleration α (dashed line). **3rd** diagram: nucleation rate $J_\star/n_{<H>}$ per second and per H–atom (solid line) and the number of dust particles per H–atom $n_d/n_{<H>}$ (dotted line). Lower diagram: condensation degree of oxygen (dark solid line), condensation degree of Ti (grey solid line) and mean radius of the dust grains (dotted line)

Two studies on the effects of grain-gas drift in non-pulsating C-rich dust driven winds have been published recently. Simis et al. (2001) presented two-fluid model calculations which covered time intervals of the order of 1000 yrs. In these models, the interaction between the dust opacity and the temperature structure was neglected and therefore, no discrete shell structure developing on a time scale of a few years was found. The authors show however, that the drift between the dust and the gas components may act as an alternative mechanism to induce semi-periodic variations in the shell structure and the mass loss rate, albeit on much longer time scales (10^2-10^3 yr) than found in models dominated by the *exterior κ-mechanism*.

Sandin & Höfner (2003) on the other hand show that grain drift can intensify the layered shell structure which results from the *exterior κ-mechanism*. In this case, the dust is more concentrated in the shocked regions in drift models and the inter-shock
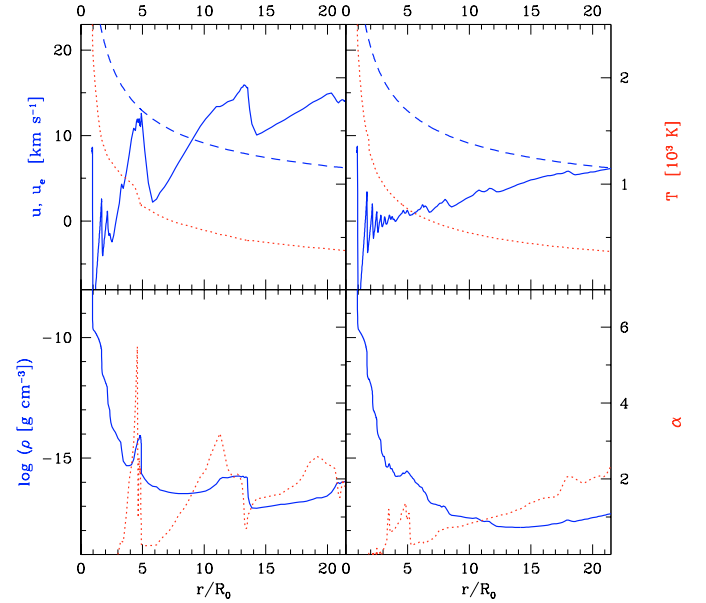
Fig. 5. Hydrodynamic structures of two model calculations with different dust opacities: the diagrams on the left display the hydrodynamic structure of model J42 with the dust opacity of Jones & Merrill (1976) and the diagrams on the right show model J59 calculated with the Draine & Lee (1984) dust opacity. Upper panel: velocity (solid line), escape velocity (dashed line), and temperature structure (dotted line). Lower panel: density (solid line) and α, the ratio of radiative acceleration to gravitational deceleration (dotted line).

regions are more depleted of dust than in the case of position coupled models. Sandin & Höfner (2003) show that, at least for massive winds, the global characteristics (mass loss rate, outflow velocity) are about the same as in single fluid models. Their models however are calculated for a time lapse of about 100 yrs only and, therefore, cannot assess variations on the time scales found by Simis et al. (2001).

An investigation of the effects of drift on the long-term evolution of pulsating dust forming wind models would require to combine a proper description of two-fluid hydrodynamics, dust formation and radiative transfer (in order not to artificially suppress the *exterior κ-mechanism*) in a pulsating atmosphere and to follow such a calculation for a sufficiently long time.

4.2. Chemical composition of dust

Contrary to the C–rich case where homogeneous dust formation occurs, i.e. the dust nuclei and the growth species are composed of the same element, dust formation in O–rich environments is a heterogeneous process.

The mass fraction of different solid components contained in the dust grains, $n_i m_i/\Sigma_i n_i m_i$, is depicted in Fig. 6 for model J42. For a compound or an element i, n_i is the number density of the entity contained in grains, and m_i is the mass of one unit of that entity. It can be seen from Fig. 6 that the composition of the grains varies considerably in the inner region of the CDS (between $2 R_0$, to $10 R_0$), due to the strong dependence of the growth process on the local density and temperature.

The variation of the chemical composition of the dust grains can be separated into three zones: (i) nucleation and
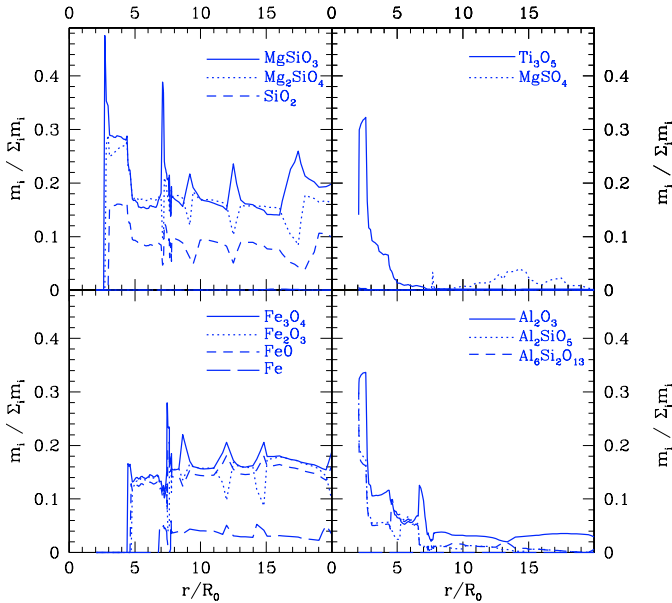
Fig. 6. Radial distribution of the mass fraction of growth species contained in dust grains for model J42 at $t = 160.0$ P.

Fig. 7. Radial distribution of the mass fraction of elements contained in dust grains for model J42 at $t = 160.0$ P.

growth of Ti–oxides and Al–oxides, (ii) growth of Mg–Si–oxides, and (iii) growth of iron compounds.

At the inner edge of dust shell, $r \sim 2\,R_0$, the growth compounds contained in dust grains mostly consist of aluminum oxides (Al_2O_3, Al_2SiO_4, $Al_6Si_2O_{13}$) and titanium oxides (e.g. Ti_3O_5). The mass fraction of titanium oxides in the grains is up to 30% in the inner region $r \sim 2$–$3\,R_0$, whereas their mass fraction becomes negligible at the regions $r > 5\,R_0$ as compared with those of Mg–Si oxides. This is mainly due to the low abundance of titanium, $\sim 10^{-4}\,\varepsilon_O$ and also because TiO_2 is consumed in the nucleation process. The Mg–Si oxides, e.g. $MgSiO_3$, Mg_2SiO_4, and SiO_2 follow the formation of aluminum oxides and become the dominant compounds in the dust. The contribution of iron species becomes important outside of $r \sim 5\,R_0$ where temperatures are low enough for the formation of iron oxides, $T < 700\,K$ (e.g. Gail & Sedlmayr 1999). The mass fraction of iron oxides in the grains reaches 40% at the outer boundary of the shell, whereas pure Fe represents only about 4% of the mass fraction of dust. The mass fraction of sulfur is generally negligibly small in the inner region, but in the outer regions, $>30\,R_0$, it reaches often up to 10% of the total mass of the grains.

In Fig. 7, the mass fraction of each element contained in dust grains is presented as a function of distance from the central star.

At $r \sim 2.5\,R_0$ just after the onset of dust formation, the mass fraction of elements contained in dust grains is mainly from O (44%), Al (30%), Ti (21%) and Si (4%). At $r \sim 4.5\,R_0$, the mass fraction of elements in dust grains is O (47%), Si (22%), Mg (16%), Al (10%), and Ti (5%). In this region there is still no relevant contribution of iron to the dust grains.

In the outer regions at $T \sim 500\,K$, most of the mass contribution by elements to dust grains is from O (36%) and Fe (36%). Si (14%) and Mg (10%) have similar contributions, whereas the contributions of Al (2%) and Ti (<1%) become les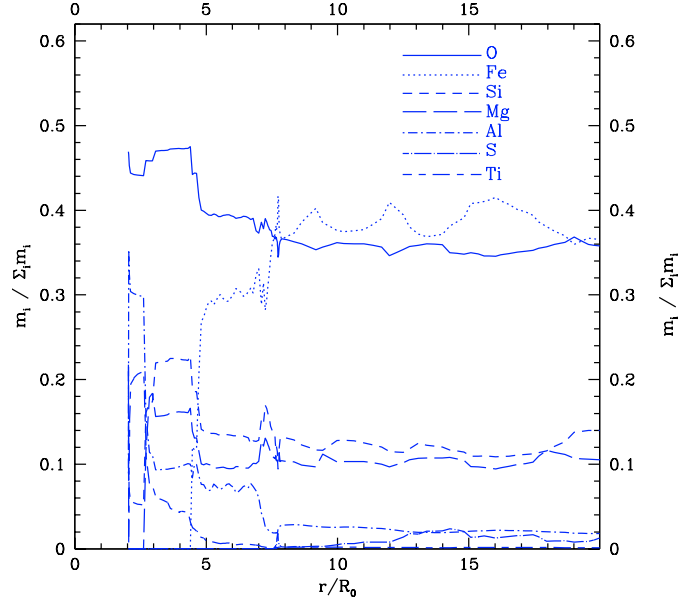s important than in the inner regions. The mass fraction of iron contained in the dust grains becomes comparable to that of oxygen because it has a 3.2 times larger mass than oxygen. With decreasing temperature, less than 400 K, the contribution of sulfur (2%) becomes as large as Al.

In the O–rich case, the chemical composition of dust grains depends on the abundances of the less abundant elements, as long as oxygen is available in the gas phase, since oxygen is not depleted and mostly is present as H_2O. For S type stars ($0.6 < C/O < 1.1$), the C/O ratio has a direct influence on dust formation and the abundance of oxygen becomes crucial for determining the dust forming species (Ferrarotti & Gail 2001, 2002).

This study on the chemical composition of the dust grains can provide us interesting insight both (a) into the sorts of species injected into the ISM and (b) into the structure of the outflows, especially in the inner region of the CDS where the wind is initiated.

O–rich dust grains generally show a lower extinction efficiency than carbonaceous grains, though the formation of O–rich dust is correspondingly efficient. Many O–rich solid particles are rather transparent (*glassy*) in the optical and near IR, but opaque in the mid IR and much less susceptive to the incident radiation field and therefore, cooler than the gas. This difference in temperatures among diverse solid particles might lead to thermal non–equilibrium effects affecting the stability sequences of dust (Patzer et al. 1998) and therefore, oxides such as TiO_2 and Al_2O_3 can already be stable in regions much closer to the central star than the silicates (Woitke 1999). Consequently dust formation might occur closer to the central star.

Impurities in the dust grains, on the other hand, seem to reduce the *glassy* characteristics and cause a strong increase of the optical extinction (e.g. Dorschner et al. 1995) which reduces in turn the thermodynamic stability of the solid and increases the internal dust temperatures.
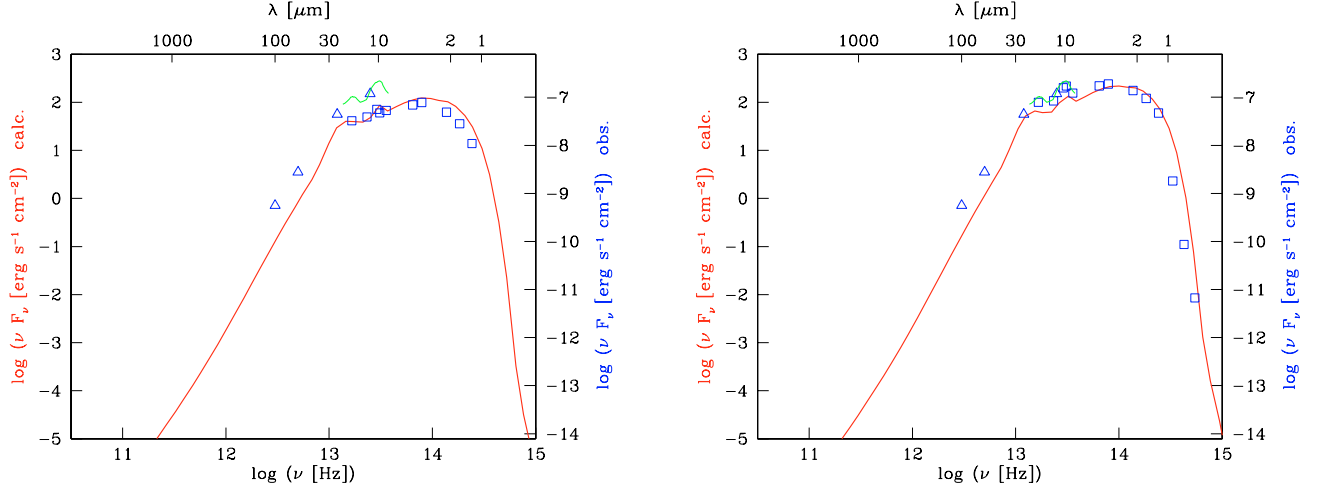
Fig. 8. Spectral energy distribution of IRC –20197 at a minimum phase (left diagram) and at a maximum phase (right diagram). The symbols are the IRAS data (triangles) and the NIR and MIR observations by Le Sidaner & Le Bertre (1993) (squares).

4.3. Spectral energy distribution

Figure 8 depicts the synthetic SEDs at a minimum (l.h.s.) and a maximum (r.h.s.) phase of the light curve. Symbols represent the near– (NIR) and mid–IR (MIR) observations obtained by Le Sidaner & Le Bertre (1993) (open squares) at JD~2446454 (minimum, l.h.s) and at JD~2446778 (maximum, r.h.s) and IRAS data (triangles) at wavelengths of 12 μm, 25 μm, 60 μm, and 100 μm at light maximum. Comparing the synthetic radiative flux through the outer shell boundary (the l.h.s. ordinate) to the observed flux on earth (the r.h.s. ordinate), we can derive the distance d to IRC –20197 from geometrical dilution of the radiation energy

$$R^2 F_{\nu,\text{calc.}} = d^2 F_{\nu,\text{obs.}}. \tag{5}$$

For our model this yields a value of $d = 1100$ pc in good agreement with our previous estimate (Table 1). The outer shell boundary of the model is located at $R = 2000 R_0 = 1.04 \times 10^{17}$ cm.

The overall agreement between calculated and observed SEDs at different phases (at minimum and at maximum phase) is satisfactory, especially in the near– and mid infrared. The IRAS data plotted in Fig. 8 refers to near maximum phase only.

4.4. Lightcurves

In Fig. 9, the synthetic light curves of the dust shell model for IRC –20197 are presented at different wavelengths over a time interval of 20 pulsational periods. The NIR observations by Le Sidaner & Le Bertre (1993) are depicted by open triangles with average magnitude of $< m_J > = 5.45$ at $\lambda = 1.24\,\mu$m (J), $< m_H > = 3.87$ at $\lambda = 1.63\,\mu$m (H), $< m_K > = 2.49$ at $\lambda = 2.19\,\mu$m (K), $< m_{L'} > = 0.42$ at $\lambda = 3.79\,\mu$m (L'), and $< m_M > = -0.09$ at $\lambda = 4.64\,\mu$m (M).

The synthetic lightcurves at wavelengths shorter than 2 μm fit excellent to the observations, whereas at longer wavelengths the amplitudes of the synthetic lightcurves become smaller than the observed ones.
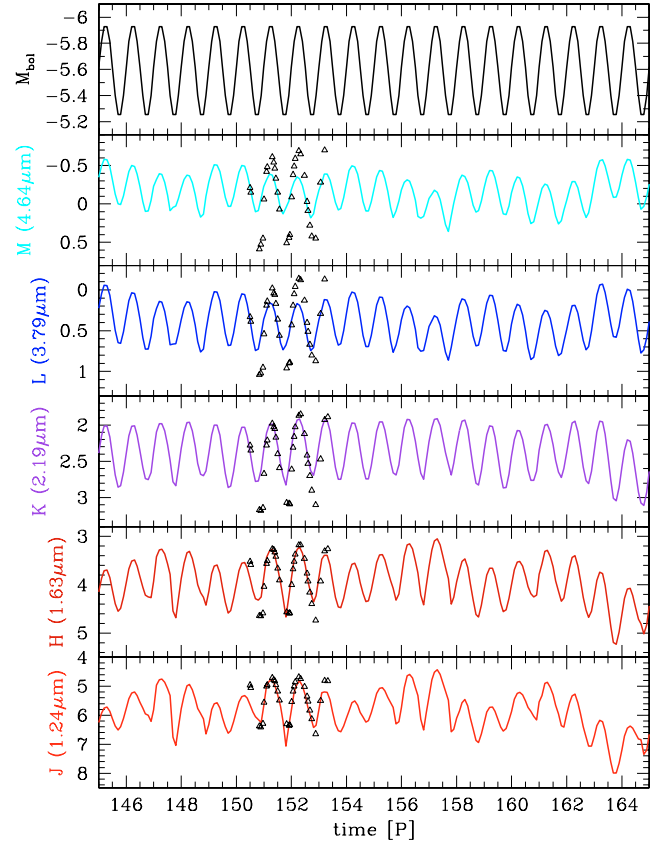

Fig. 9. Synthetic lightcurves of the dust shell model (solid lines) at different wavelengths over a time interval of 20 pulsational periods and the observed light curves (symbols) of IRC –20197 at $\lambda = 1.24\,\mu$m (J) $\lambda = 1.63\,\mu$m (H), $\lambda = 2.19\,\mu$m (K), $\lambda = 3.79\,\mu$m (L'), and $\lambda = 4.64\,\mu$m (M) (Le Sidaner & Le Bertre 1993). The lightcurves are plotted in absolute magnitude at each wavelength.

While the synthetic bolometric luminosity plotted in the upper diagram of Fig. 9 shows strict sinusoidal behaviour, the light curves at different wavelengths exhibit non–sinusoidal behaviour. This long term variation in the lightcurves is caused by the formation of new dust layers on time scales larger than the
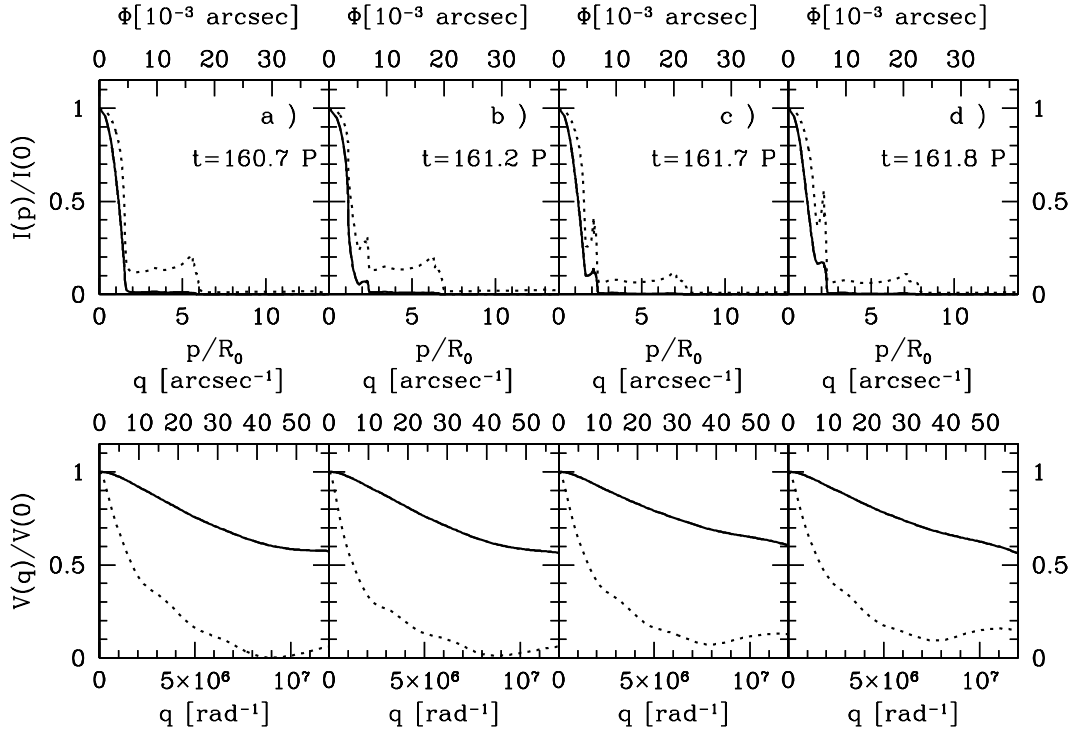
Fig. 10. Intensity profiles (upper diagram) and the corresponding visibility functions (lower diagram) in the inner regions of the dust shell model J42 for $\lambda = 2.2\,\mu$m (solid lines) and $\lambda = 12\,\mu$m (dotted lines) for different instants of time.

pulsation period of the star. The eigen–timescale which occurs in the hydrodynamic structure is ~5 P and this is clearly seen at wavelengths shorter than the K band.

4.5. Spatial spectra

Based on the hydrodynamic structures of model J42, the synthetic intensity profiles $I(p)$ of the dust shell model and the resulting visibility functions $V(q)$ at two different wavelengths, 2 μm and 12 μm, are depicted in Fig. 8 at different instants of time. Columns (a) and (b) correspond to the time instants of light minimum and light maximum in Fig. 8.

The temporal evolution of the dust layers can be seen in the intensity profiles in Fig. 10. The intensity and corresponding visibility at 2 μm is mainy dominated by the central star, whereas at 12 μm, the step–like behaviour of the dust shells in the intensity and visibility is clearly seen. At $t = 160.20\,$P a maximum phase of light curve corresponds to a phase, when a newly formed dust layer starts to develop which corresponds to minimum of optical depth. At wavelength 12 μm, the location of dust layers is clearly indicated by steps and these structures are caused by the thermal emission of dust concentrated in the layers. The layers in O–rich CDSs occur less frequent and are broader than in the C–rich case.

In Fig. 11, we plotted the intensity profiles and the corresponding visibilities for model J42 at 2 different time instants 5 P apart. After this eigen–timescale, ~5 P, the hydrodynamic structure repeats itself, which is also reflected in the lightcurves. Intensity profiles and visibilities at 12 μm serve as a better tool than those at 2.2 μm to find this timescale of the CDS.

The circumstellar structure of model J59 behaves almost stationary, its eigen–timescale approaches infinity. As a result, also its intensity profiles and corresponding visibilities almost do not change in time. This is mainly because the dust formation is not effective in its CDS and the model therefore, does not produce distinct dust layers in the hydrodynamic structure. The comparison of the intensities and visibilities between model J42 and model J59 is shown in Fig. 12. Here again, intensities and visibilities at 12 μm provide clear differences and therefore, we can take the visibility at 12 μm as a good tool to discriminate between the different dust opacities.

4.6. Comparison of $\dot{M}$ vs. color indices with the empirical relations

Observations show that there exists a clear correlation between mass loss rates and IR color indices (CI) (Whitelock et al. 1994; Le Sidaner & Le Bertre 1996; Le Bertre & Winters 1998). These correlations between IR CIs and mass loss rates for Mira stars are distance–independent and therefore, can provide an easy-to-use tool to measure directly mass loss rates via IR CIs.

Based on the time–dependent model calculations for IRC –20197 with the fundamental parameters given in Table 5, we compare the model results of $\dot{M}/(J - K)$ and of $\dot{M}/(K - L')$ with the empirical relations in Fig. 13. The symbols represent the model calculations and the dashed lines give the empirical relations in Le Bertre & Winters (1998). The resulting values from the model calculations for IRC –20197 show good agreement with the empirical relations for both CIs, $J - K$ and $K - L'$ for $1.6 \le J - K \le 6.0$ and $0.7 \le K - L' \le 3.0$.
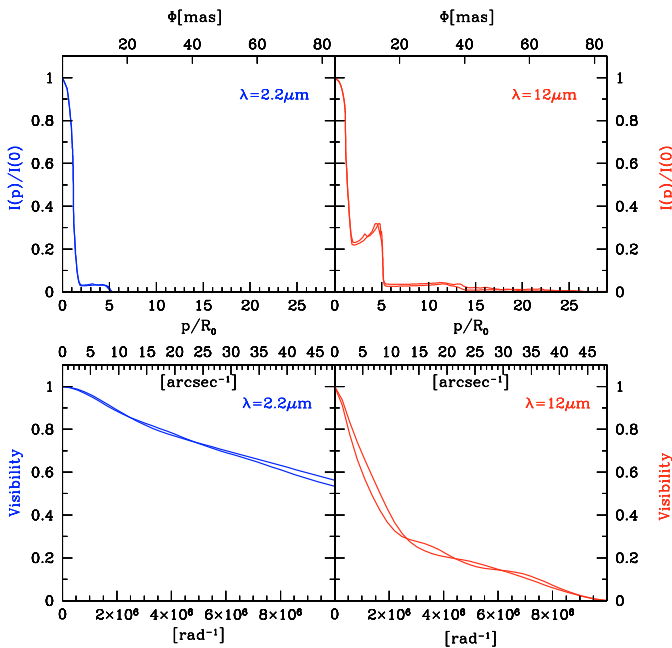
Fig. 11. Intensity profiles in the inner regions (upper diagram) and the corresponding visibility functions (lower diagram) of the dust shell model J42 at $\lambda = 2.2\,\mu m$ and $\lambda = 12\,\mu m$ for different time instants (155 P and 160 P), separated by a time interval of 5 P.

Fig. 12. Intensity profiles in the inner regions (upper diagram) and the corresponding visibility functions (lower diagram) at $\lambda = 2.2\,\mu m$ and $\lambda = 12\,\mu m$ and at a time instant of $t = 160.7$ P (light minimum) for model J42 (solid line) and for model J59 (dotted line).

The results from the model calculations with Draine & Lee opacity generally show deviations from the empirical relations between $\dot{M}$ and CIs, especially for CIs such as $J-K$ and $K-L'$.

Covering the typical parameter range relevant to AGB stars, synthetic $\dot{M}$ vs. CI relations have been presented and discussed in Jeong et al. (2002). Further discussions will be presented in a forthcoming study (Jeong et al., in preparation).

5. Conclusions

In this paper, we present a self–consistent time–dependent model for the dust forming O–rich AGB star IRC –20197 undergoing mass loss at a large rate ($\geq 10^{-6}\,M_\odot\ \mathrm{yr}^{-1}$). The model includes a consistent treatment of the interactions among hydrodynamics, thermodynamics, radiative transfer, equilibrium chemistry, and *heterogeneous* dust formation. We consider TiO_2 as nucleation seed. This is the first dynamic model calculation with time dependent dust formation in CDS around O–rich AGB stars.

The radial structures of time–dependent O–rich CDS models show characteristics similar to the C–rich case (Fleischer et al. 1992; Winters et al. 2000).The CDS exhibits a discrete layered structure and the dust is distributed inhomogeneously and concentrated in discrete layers. The dust layers are typically correlated with the hydrodynamic structure. The strong shocks propagating through the shell are accelerated by radiation pressure on dust and produce a distinct layered density structure which in turn provides favorable conditions for dust growth. The radial structure of the temperature is characterized by a *back–warming effect* by which the material below the dust layers is heated due to the thermal re–emission of the dust grains. This effect influences decisively the
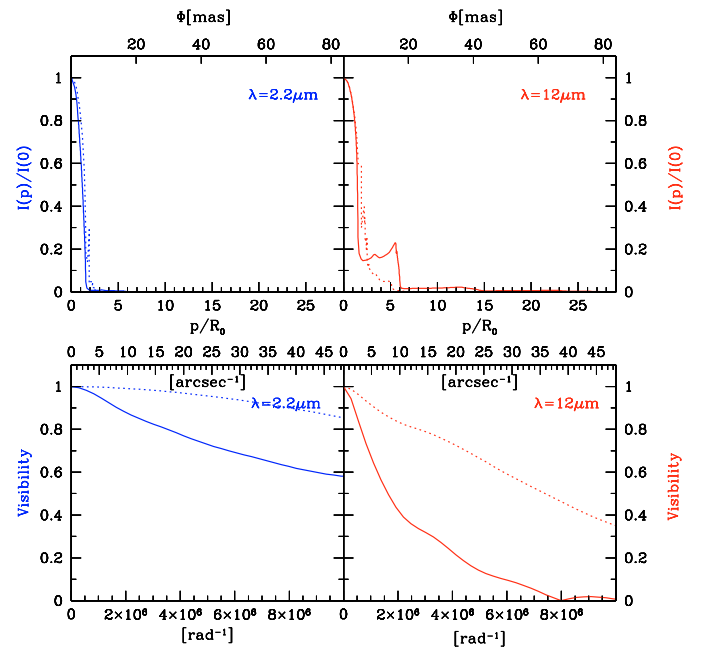
nucleation which steeply depends on temperature. The formation of new dust layers possesses its *eigen–period*, which is generally longer than the pulsation period of the star and consequently introduces the effect of *multiperiodicity* (Fleischer et al. 1995).

We probe this model by doing a detailed comparison with a well observed O–rich Mira variable, IRC –20197. The model is determined by the stellar parameters of the hydrostatic initial model with stellar mass $M_\star = 1.3\,M_\odot$, stellar luminosity $L_\star = 1.4 \times 10^4 \times L_\odot$, stellar temperature $T_\star = 2400\,K$, and solar abundances of the elements and the pulsation of the star is simulated by a piston at the inner boundary where the velocity varies sinusoidally with a period of $P = 636$ d and an amplitude of $\Delta v_\mathrm{p} = 8\,\mathrm{km\,s}^{-1}$. In order to get a model which reproduces the observations of IRC –20197, we described the dust opacity by the extinction efficiencies given by Jones & Merrill (1976) which are relevant to *circumstellar* dust. With opacities derived for interstellar dust we could not obtain any satisfactory model for IRC –20197.

The model yields a time averaged outflow velocity of $11.9\,\mathrm{km\,s}^{-1}$ and an average mass loss rate of $7.3 \times 10^{-6}\,M_\odot\ \mathrm{yr}^{-1}$ which are in good agreement with the values derived from radio observations. The resulting dust–to–gas ratio is $\rho^\mathrm{d}/\rho^\mathrm{g} = 3.5 \times 10^{-3}$. Comparing the synthetic SEDs with the observed ones, we derive a distance of 1.1 kpc to IRC –20197 which is in good agreement with previous estimates (Le Bertre & Winters 1998).

The chemical composition of the grains given in mass fraction of the contributing elements varies in the CDS from $2\,R_0$ to $10\,R_0$ and shows three zones of different chemical composition. In the starting zone of dust formation, dust consists of mainly O, Al, and Ti. Between $2\,R_0$ and $5\,R_0$, the contribution of Mg
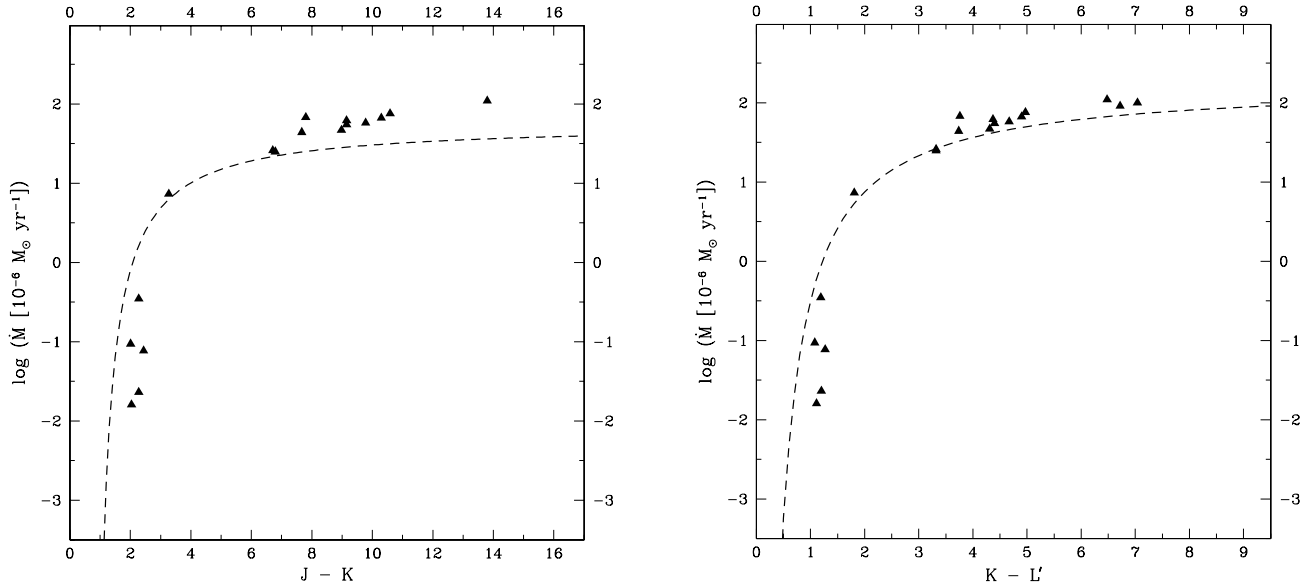
Fig. 13. Comparison of $\dot{M}/(J − K)$ (l.h.s.) and $\dot{M}/(K − L')$ (r.h.s) to the empirical relations (Le Bertre & Winters 1998) for $1.6 \leq J − K \leq 6.0$ and $0.7 \leq K − L' \leq 3.0$. Symbols represent the model calculations, and the dashed lines give the empirical relations.

and Si increases substancially. Still there is no relevant contribution of iron. At $r > 5\,R_0$ where the temperature becomes lower than 1000 K, iron contributes substantially to the mass of the dust grains in form of oxides and it becomes even comparable to that of oxygen, at the outer boundary. Sulfur contributes only ~2% at the outer boundary.

We also present the synthetic light curves at different wavelengths. The synthetic SEDs at different phases of the pulsation cycle and the synthetic light curves at different wavelengths show good agreement with the IR observations of IRC −20197. The calculated luminosity is of sinusoidal behaviour, whereas the lightcurves at different wavelengths reflect *multiperiodicity* of the hydrodynamic structure. For model J42, the eigen–timescale, ~5 P of the hydrodynamic structure is clearly seen in its lightcurves at different wavelengths. At wavelengths shorter than the K band, the light curves are in excellent agreement with the observed lightcurves. At wavelengths longer than the K band, the amplitudes of the lightcurves become smaller than observed, which is also seen in the synthetic bolometric luminosity.

The synthetic intensity profiles and visibilities are also presented for IRC −20197 at different wavelengths. The intensity and visibility at 12 μm provide a better tool than at other wavelengths to study the temporal variation of the dust shell. In the synthetic intensity profiles, the eigen–timescale of the hydrodynamic structure is clearly seen.

We have probed our model on the source IRC −20197 and have obtained a satisfactory agreement with the observations. This success gives support to our modeling approach. The models that we have developed for the O–rich Mira IRC −20197 show also an excellent agreement with the correlations between $\dot{M}$ and CIs derived from observations (Le Bertre & Winters 1998). In a forthcoming paper, we will use our model to systematically investigate the properties of O–rich outflows and in particular discuss the relations between mass loss rate and CIs.

References

Andersen, A., Loidl, R., & Höfner, S. 1999, A&A, 349, 243
Arndt, T. U., Fleischer, A. J., & Sedlmayr, E. 1997, A&A, 327, 614
Beck, H. K. B., Gail, H.-P., Henkel, R., & Sedlmayr, E. 1992, A&A, 265, 626
Begemann, B., Dorschner, J., Henning, T., et al. 1997, ApJ, 476, 199
Chang, C., Patzer, A. B. C., Sedlmayr, E., Steinke, T., & Sülzle, D. 2000, Chem. Phys. Lett., 324, 108
Chang, C., Patzer, A. B. C., Sedlmayr, E., & Sülzle, D. 1998, Eur. Phys. J. D, 2, 57
Danchi, W. C., Bester, M., Degiacomi, C. G., Greenhill, L. J., & Townes, C. H. 1994, AJ, 107, 1469
DeGioia-Eastwood, K., Hackwell, J. A., Grasdalen, G. L., & Gehrz, R. D. 1981, ApJ, 245, L75
Demyk, K., Carrez, P., Leroux, H., et al. 2001, A&A, 368, L38
Dominik, C., Sedlmayr, E., & Gail, H.-P. 1993, A&A, 277, 578
Dorschner, J., Begemann, B., Henning, T., Jaeger, C., & Mutschke, H. 1995, A&A, 300, 503
Draine, B. T. 1985, ApJS, 57, 587
Draine, B. T., & Lee, H. M. 1984, ApJ, 285, 89
Fabian, D., Posch, T., Mutschke, H., Kerschbaum, F., & Dorschner, J. 2001, A&A, 373, 1125
Feast, M. W. 1996, MNRAS, 278, 11
Ferrarotti, A. S., & Gail, H.-P. 2001, A&A, 371, 133
Ferrarotti, A. S., & Gail, H.-P. 2002, A&A, 382, 256

Fleischer, A. J., Gauger, A., & Sedlmayr, E. 1991, A&A, 242, L1

Fleischer, A. J., Gauger, A., & Sedlmayr, E. 1992, A&A, 266, 321

Fleischer, A. J., Gauger, A., & Sedlmayr, E. 1995, A&A, 297, 543

Fleischer, A. J., Winters, J. M., & Sedlmayr, E. 1999, in Asymptotic Giant Branch Stars, ed. T. Le Bertre, A. Lèbre, & C. Waelkens (ASP), IAU Symp., 191, 187

Gail, H.-P., Keller, R., & Sedlmayr, E. 1984, A&A, 133, 320

Gail, H.-P., & Sedlmayr, E. 1986, A&A, 166, 225

Gail, H.-P., & Sedlmayr, E. 1998a, in The Molecular Astrophysics of Stars and Galaxies, ed. T. Hartquist, & D. Williams (Oxford, GB: Oxford Science Pub.), 285

Gail, H.-P., & Sedlmayr, E. 1998b, in Chemistry and physics of molecules and grains in space, Faraday Discussion No. 109, ed. P. Sarre (London, GB), 303

Gail, H.-P., & Sedlmayr, E. 1999, A&A, 347, 594

Goeres, A., Henkel, R., Sedlmayr, E., & Gail, H.-P. 1988, Rev. Mod. Astron., 1, 231

IRAS Science Team 1986, A&AS, 65, 607

Höfner, S. 1999, A&A, 346, L9

Höfner, S., Feuchtinger, M. U., & Dorfi, E. A. 1995, A&A, 297, 815

Höfner, S., Gautschy–Loidl, R., Aringer, B., & Jørgensen, U. G. 2003, A&A, 399, 589

Höfner, S., Jørgensen, U. G., Loidl, R., & Aringer, B. 1998, A&A, 340, 497

Jeong, K. S. 2000, Ph.D. Thesis, Technische Universität, Berlin, Germany

Jeong, K. S., Chang, C., Sedlmayr, E., & Sülzle, D. 2000, J. Phys. B, 33, 3417

Jeong, K. S., Winters, J. M., Le Bertre, T., & Sedlmayr, E. 2002, in Mass-losing Pulsating Stars and their Circumstellar Matter, ed. Y. Nakada, M. Honma, & M. Seki (Dordrecht: Kluwer), 139

Jeong, K. S., Winters, J. M., & Sedlmayr, E. 1999, in IAU Symp. 191: Asymptotic Giant Branch Stars, ed. T. Le Bertre, A. Lèbre, & C. Waelkens (ASP), 233

John, M. 1995, Master's thesis, Technische Universität, Berlin, Germany

John, M., & Sedlmayr, E. 1997, Astrophys. Space Sci., 251, 219

Jones, A. P., Tielens, A. G. G. M., & Hollenbach, D. J. 1996, ApJ, 469, 740

Jones, T. W., & Merrill, K. M. 1976, ApJ, 209, 509

Kastner, J. H. 1990, Ph.D. Thesis, California Univ., Los Angeles, USA (K90)

Knapp, G., Young, K., Lee, E., & Jorissen, A. 1998, ApJS, 117, 209 (KYLJ98)

Köhler, T. M., Gail, H.-P., & Sedlmayr, E. 1997, A&A, 320, 553

Kozasa, T., & Hasegawa, H. 1987, Prog. Theor. Phys., 77, 1402

Le Bertre, T. 1993, A&AS, 97, 729

Le Bertre, T., & Winters, J. M. 1998, A&A, 334, 173 (LW98)

Le Sidaner, P., & Le Bertre, T. 1993, A&A, 278, 167 (Paper I)

Le Sidaner, P., & Le Bertre, T. 1996, A&A, 314, 896

Loup, C., Forveille, T., Omont, A., & Paul, J. F. 1993, A&AS, 99, 291 (LFOP93)

Nittler, L. R., Alexander, C. M. O. D., Gao, X., Walker, R. M., & Zinner, E. 1997, ApJ, 483, 475

Nuth, J. A., & Donn, B. 1982, J. Chem. Phys., 77, 2639

Olofsson, H. 1999, in Asymptotic Giant Branch Stars, ed. T. Le Bertre, A. Lèbre, & C. Waelkens (ASP), IAU Symp., 191, 3

Onaka, T., de Jong, T., & Willems, F. J. 1989, A&A, 218, 169

Ossenkopf, V., Henning, Th., & Mathis, J. S. 1992, A&A, 261, 567

Patzer, A. B. C. 1998, Ph.D. Thesis, Technische Universtät Berlin, Berlin, Germany

Patzer, A. B. C., Chang, C., Sedlmayr, E., & Sülzle, D. 1999, Eur. Phys. J. D, 6, 57

Patzer, A. B. C., Gauger, A., & Sedlmayr, E. 1998, A&A, 337, 847

Perrin, G., Coudé du Foresto, V., Ridgway, S. T., et al. 1998, A&A, 331, 619

Platt, J. R. 1956, ApJ, 123, 486

Posch, T., Kerschbaum, F., Mutschke, H., et al. 1999, A&A, 352, 609

Rittner, E. S. 1951, J. Chem. Phys., 19, 1030

Sandin, C., & Höfner, S. 2003, A&A, 398, 253

Sedlmayr, E. 1989, in Interstellar Dust, ed. L. J. Allamandola, & A. G. G. M. Tielens (Dordrecht: Kluwer Academic Publishers), 467

Sedlmayr, E. 1994, in Molecules in the Stellar Environment, ed. U. G. Jørgensen (Berlin: Springer–Verlag), IAU Coll., 146, 163

Sedlmayr, E., & Winters, J. M. 1997, Stellar Atmospheres: Theory and Observations, Vol. 497 of Lecture Notes in Physics, ed. J.-P. De Greve, R. Blomme, & H. Hensberge (EADN Astrophysics School IX–Brussels, Springer), 89

Simis, Y. J. W., Icke, V., & Dominik, C. 2001, A&A, 371, 205

Sogawa, H., & Kozasa, T. 1999, ApJ, 516, L33

Speck, A. K., Barlow, M. J., Sylvester, R. J., & Hofmeister, A. M. 2000, A&AS, 146, 437

Tielens, A. G. G. M. 1990, in From Miras to Planetary Nebulae: Which path for stellar evolution?, ed. M. O. Mennessier, & A. Omont (Gif sur Yvette Cedex – France: Éditions Frontières), 186

Wachter, A. C., Schröder, K.-P., Winters, J. M., Arndt, T. U., & Sedlmayr, E. 2002, A&A, 384, 452

Waters, L. B. F. M., Molster, F. J., de Jong, T., et al. 1996, A&A, 315, L361

Whitelock, P., Menzies, J., Feast, M., et al. 1994, MNRAS, 267, 711

Winters, J. M., Dominik, C., & Sedlmayr, E. 1994, A&A, 288, 255

Winters, J. M., Fleischer, A. J., Gauger, A., & Sedlmayr, E. 1995, A&A, 302, 483

Winters, J. M., Fleischer, A. J., Le Bertre, T., & Sedlmayr, E. 1997, A&A, 326, 305

Winters, J. M., Le Bertre, T., Jeong, K. S., Helling, C., & Sedlmayr, E. 2000, A&A, 361, 641

Woitke, P. 1999, in Astronomy with Radioactivities, ed. R. Diehl, & D. Hartmann (Schloß Ringberg, Germany: MPE Report 274), 163

Woitke, P., Dominik, C., & Sedlmayr, E. 1993, A&A, 274, 451

Zinner, E. 1998, Ann. Rev. Earth Planet. Sci., 26, 147

Zuckerman, B., & Dyck, H. M. 1986, ApJ, 304, 394